ADVANCED MATERIALS
www.advmat.de

Highly Sensitive and Cost-Effective Polymeric-Sulfur-Based Mid-Wavelength Infrared Linear Polarizers with Tailored Fabry–Pérot Resonance

Woongbi Cho, Jehwan Hwang, Sang Yeon Lee, Jaeseo Park, Nara Han, Chi Hwan Lee, Sang-Woo Kang, Augustine Urbas, Jun Oh Kim, Zahyun Ku, and Jeong Jae Wie**

Inverse-vulcanized polymeric sulfur has received considerable attention for application in waste-based infrared (IR) polarizers with high polarization sensitivities, owing to its high transmittance in the IR region and thermal processability. However, there have been few reports on highly sensitive polymeric sulfur-based polarizers by replication of pre-simulated dimensions to achieve a high transmission of the transverse magnetic field (T_{TM}) and extinction ratio (ER). Herein, a 400-nanometer-pitch mid-wavelength infrared bilayer linear polarizer with self-aligned metal gratings is introduced on polymeric sulfur gratings integrated with a spacer layer (SM-polarizer). The dimensions of the SM-polarizer can be closely replicated using pre-simulated dimensions via a systematic investigation of thermal nanoimprinting conditions. Spacer thickness is tailored from 40 to 5100 nm by adjusting the concentration of polymeric sulfur solution during spin-coating. A tailored spacer thickness can maximize T_{TM} in the broadband MWIR region by satisfying Fabry–Pérot resonance. The SM-polarizer yields T_{TM} of 0.65, 0.59, and 0.43 and ER of 3.12×10^3, 5.19×10^3, and 5.81×10^3 at 4 µm for spacer thicknesses of 90, 338, and 572 nm, respectively. This demonstration of a highly sensitive and cost-effective SM-polarizer opens up exciting avenues for infrared polarimetric imaging and for applications in polarization manipulation.

1. Introduction

Since the first report on inverse vulcanization of elemental sulfur in 2013,[1] polymeric sulfur has received considerable attention in various fields, including thermal imaging,[2–5] energy storage applications,[6–8] and triboelectric nanogenerators.[9,10] As elemental sulfur is a by-product of petroleum-refining processes that generate a vast annual surplus of 7 million tons, low-cost mass production of polymeric sulfur is feasible.[11] Furthermore, polymeric sulfur is recyclable, owing to its dynamic covalent disulfide bonds.[4,12] In particular, the elemental-sulfur-based backbone of polymeric sulfur exhibits a high intrinsic transmittance in the infrared (IR) region, unlike organic carbon-based polymers.[4,5,12] These advantages make polymeric sulfur a promising alternative to brittle, heavy, and expensive inorganic compounds or chalcogenides

W. Cho, J. J. Wie
Department of Organic and Nano Engineering
Hanyang University
222 Wangsimmni-ro, Seongdong-gu, Seoul 04763, Republic of Korea
E-mail: jjwie@hanyang.ac.kr

J. Hwang, C. H. Lee
Weldon School of Biomedical Engineering
Purdue University
West Lafayette, IN 47907, USA

S. Y. Lee
Department of Polymer Science and Engineering
Inha University
100 Inha-ro, Michuhol-gu, Incheon 22212, Republic of Korea

J. Park, S.-W. Kang, J. O. Kim
Advanced Instrumentation Institute
Korea Research Institute of Standards and Science
267 Gajeong-ro, Yuseong-gu, Daejeon 34113, Republic of Korea

J. Park, S.-W. Kang
Precision Measurement
University of Science and Technology (UST)
267 Gajeong-ro, Yuseong-gu, Daejeon 34113, Republic of Korea

The ORCID identification number(s) for the author(s) of this article can be found under https://doi.org/10.1002/adma.202209377.

DOI: 10.1002/adma.202209377

N. Han
Program in Environmental and Polymer Engineering
Inha University
100 Inha-ro, Michuhol-gu, Incheon 22212, Republic of Korea

N. Han, J. J. Wie
Department of Chemical Engineering
State University of New York College of Environmental Science and Forestry
Syracuse, NY 13210, USA

C. H. Lee
School of Mechanical Engineering
Purdue University
West Lafayette, IN 47907, USA

C. H. Lee
School of Materials Engineering
Purdue University
West Lafayette, IN 47907, USA

C. H. Lee
Birck Nanotechnology Center
Purdue University
West Lafayette, IN 47907, USA

A. Urbas, Z. Ku
Materials and Manufacturing Directorate
Air Force Research Laboratory
Wright-Patterson Air Force Base, Dayton, OH 45433, USA
E-mail: zahyun.ku.1.ctr@us.af.mil

such as Ge, KBr, KRS-5, GaAs, ZnSe, ZnS, BaF_2, and CaF_2, which are commonly used for mid-wavelength infrared (MWIR) optics.[13,14] Moreover, the aforementioned conventional inorganics require an expensive process—interference lithography—to fabricate highly sensitive IR polarizers for high-end applications.[15–17] However, polymeric sulfur has temperature-dependent rheological properties that enable thermal processability; therefore, it can be used for the cost-effective thermal fabrication (i.e., thermal nanoimprinting) to prepare IR polarizers.[18,19]

For a high-quality polarimetric image, polarization sensitivity is crucial for distinguishing the object from complex natural backgrounds by obtaining additional information such as shading and surface morphologies.[20–25] For highly sensitive polarizers, both a high transmission of the transverse magnetic field (T_{TM}) and a high extinction ratio (ER) are required in the broadband wavelength region to achieve high polarization sensitivity. The ER represents the separation performance from unpolarized to polarized light, obtained by dividing the T_{TM} by the transmission of the transverse electric field (T_{TE}). An ideal polarizer would have an infinite ER, because it would completely penetrate the transverse magnetic field (TM) and block the transverse electric field (TE);[26] thus, an ideal polarizer could provide the desired additional information with high contrast. Recently, polymeric sulfur has been used to prepare MWIR linear polarizers via a 2-step process involving thermal nanoimprinting lithography (NIL) and metal deposition.[22,23] To achieve a bilayer wire-grid polarizer structure, 1D nano-gratings were integrated with a spacer layer based on polymeric sulfur via thermal NIL, and metal deposition was subsequently used to achieve self-aligned metallic wire-grid gratings. However, these two reports have only fabricated polarizers with pitches larger than 700 nm that cannot maximize ER and have limitations with high-quality replicating the pre-simulated target dimensions that assure the high polarizer sensitivity, due to the insufficiently investigated thermal NIL process. Furthermore, these each previous studies investigated the spacer thickness that satisfied the Fabry–Pérot (F–P) resonance in broadband IR region only via numerical simulation.

For a fixed grating width and a duty cycle (width/pitch ratio), the ER of polarizer with bilayer 1D grating structure can be enhanced by reducing the wire-grid pitch because the ability to block the TE is increased.[22,27,28] Therefore, a smaller pitch is required to achieve highly enhanced polarization sensitivity.[29] However, the difficulties of high-quality replicating the smaller pitch design exponentially grow by thermal NIL, due to a drastically increased surface tension originating from the enhanced surface-area-to-volume (SA/V) ratio.[30,31] Furthermore, the high melt viscosity of polymeric sulfur can prevent complete filling of the nano-structured mold. To achieve a high-quality replication of simulated 3D geometries, the transition from the unfilled Cassie–Baxter state to the fully filled Wenzel state must be achieved by regulating thermal NIL conditions, including compression pressure, processing temperature, and time.[32,33] When thermal NIL conditions are unsuitable to overcome high surface tension and melt viscosity, a less-filled intermediate state is obtained, which imparts round-shaped upper gratings to polymeric sulfur-based 1D nano-gratings. When the metal layer is deposited on the round-shaped polymeric sulfur gratings, it resulted in the connection of upper metal layer with lower metal layer. This connection can physically block incident light from entering the polymeric sulfur spacer layer and thereby decrease T_{TM}. Hence, a systematic investigation of thermal NIL conditions is required to achieve high-fidelity polymeric sulfur-based 1D nano-gratings.

In particular, optimization of spacer layer thickness is required to achieve boosted T_{TM} in broadband IR region in polarizer with bilayer 1D grating structure. When light enters an F–P interferometer (spacer in polarizer with bilayer 1D grating) comprised of uniformly spaced parallel semi-transparent reflectors, it undergoes multiple reflections and interferences.[34] Constructive interference occurs when the phase of these numerous reflected lights matches, and this condition demonstrates F–P resonance that maximizes the T_{TM} of polarizer. This phase of reflected light is highly related to the distance between two parallel semi-transparent reflectors in the F–P interferometer. An optimal spacer thickness is required to satisfy F–P resonance in broadband IR region to achieve highly sensitive IR polarizer.[35]

In this study, we demonstrate the high-quality replication of pre-simulated dimensions in a waste-based MWIR wire-grid linear polarizer (SM-polarizer) with a pitch of ≈400 nm. The SM-polarizer has a bilayer structure constructed on a Si substrate and is composed of a self-aligned bilayer-Au-based wire-grid above the high-fidelity 1D nano-gratings integrated with a spacer layer based on polymeric sulfur. Before the fabrication of the SM-polarizer, a numerical simulation was performed to guide the effective dimensions of an SM-polarizer with a 400 nm pitch, including grating width, grating height, Au thickness, and spacer thickness. A pitch of 400 nm is significantly smaller than previous reports, making thermal NIL more difficult. To overcome this processing difficulty, we systematically investigated thermal NIL conditions, including temperature, pressure, and time in order to determine the optimal condition for high-fidelity nanofabrication of the pre-simulated design for the SM-polarizer. Thermal NIL conditions can be further fine-tuned by considering the correlation of time and pressure as explained by Stefan's squeeze flow equation and thermal behavior of polymeric sulfur including glass transition and thermal degradation. Importantly, wide range control of spacer thickness in SM-polarizer is conducted by adjusting the concentration of the polymeric sulfur solution during spin-coating

J. J. Wie
Human–Tech Convergence Program
Hanyang University
222 Wangsimmni-ro, Seongdong-gu, Seoul 04763, Republic of Korea
J. J. Wie
Institute of Nano Science and Technology
Hanyang University
222 Wangsimmni-ro, Seongdong-gu, Seoul 04763, Republic of Korea
J. J. Wie
Department of Chemical Engineering
Hanyang University
222 Wangsimmni-ro, Seongdong-gu, Seoul 04763, Republic of Korea
J. J. Wie
The Michael M. Szwarc Polymer Research Institute
State University of New York College of Environmental Science and Forestry
Syracuse, NY 13210, USA

process at a fixed spin-speed, to identify the optimal spacer thickness which satisfies the F–P resonance for broadband IR region. Finally, we employed Fourier transform infrared spectroscopy (FT-IR) measurements and simulations to investigate the optical performance of the SM-polarizer, including T_{TM}, T_{TE}, and ER. This study provides guidelines for upcycling polymeric sulfur to high-optical-performance waste-based MWIR linear polarizers via high-fidelity 1D nano-grating structures and effective F–P cavity resonance in thickness-controlled spacers.

2. Results and Discussion

2.1. Numerical Analysis to Optimize the Structural Parameters of the SM-Polarizer

To effectively guide the design of an SM-polarizer with high polarization sensitivity, we numerically simulated and theoretically analyzed its optical properties based on the geometrical parameters. The proposed structure comprises a self-aligned bilayer metallic grating (upper and lower Au gratings), spacer layer (used as the optical cavity), and Si substrate (Figure S1a, Supporting Information). The geometrical parameters of the SM-polarizer include the pitch (p), width of upper grating (w), width of lower grating (p-w), spacer thickness (t_d), grating height (t_g), and Au thickness (t_{Au}). The duty cycle (r) is defined as the ratio of the width of the upper Au grating (w) to the pitch (p). In the simulation, the transverse electromagnetic (TEM) plane wave was normally incident in the z-direction. The transverse magnetic (TM) and transverse electric (TE) modes are defined as the polarization states in which the electric field direction is perpendicular (x-direction) and parallel (y-direction) to the Au gratings, respectively. To understand the mechanism of the optical cavity in the SM-polarizer structure, we performed a theoretical analysis based on a multiple-layer model, as shown in Figure S1b (Supporting Information). When the distance between the lower Au gratings/spacer layer and the spacer layer/Si substrate satisfied the quarter-wavelength optical thickness, the transmission of TM was maximized because of the constructive interference between the incident and reflected light. The peak resonance was observed when the half-wavelength distance between the Si substrate and the lower Au gratings corresponded to the F–P mode. The F–P cavity satisfied the round-trip phase condition (γ), as expressed in Equation (1).[26,36]

$$\gamma = \phi(r_{21}) + \phi(r_{23}) - 2\beta = 2m\pi, |m| = 0, 1, 2 \quad (1)$$

where $\phi(r_{21})$ and $\phi(r_{23})$ are the reflection phases at the lower Au gratings/spacer layer interface and spacer layer/Si substrate interface, respectively, obtained from numerical simulations using CST Microwave Studio;[37] $\beta = n_{spacer} \times k \times t_d$ is the propagating phase in the cavity, where n_{spacer}, k, and t_d are the refractive index of the spacer layer, the wave vector, and the spacer thickness, respectively; and m is an integer denoting the order of the F–P resonance. The refractive indices of the substrate and spacer layer were the averages of $n_{Si} = 3.4$ and $n_{spacer} = 1.7$, respectively. The imaginary part of the refractive index (extinction coefficient: k) of the spacer layer was neglected, owing to the very low absorption coefficients. Drude model was used for Au permittivity, which is given by $\varepsilon_{Au} = 1 - \omega_p^2/\omega(\omega + i\omega_c)$, with the plasma frequency $\omega_p = 1.38 \times 10^{16}$ Hz and collision frequency $\omega_c = 5.71 \times 10^{13}$ Hz.[38]

Figure 1 shows the simulated TM transmission (T_{TM}), TE transmission (T_{TE}), and extinction ratio (ER) for spacer thickness, grating height, and duty cycle in the SM-polarizer at a pitch of 400 nm and Au thickness of 100 nm. As shown in Figure 1a, the T_{TM} spectra of the SM-polarizer are plotted as a function of the wavelength and spacer thickness (t_d) for w = 0.2 μm and t_g = 0.2 μm. When the spacer thickness increases from 0.05 to 6 μm, the higher-order resonance peaks appear with ten resonance modes (white dashed lines) corresponding to ten peak wavelengths, which is consistent with the calculations obtained using Equation (1). The T_{TE} (Figure 1b) also exhibits a resonance peak as the spacer thickness increases, and the ER (Figure 1c) fluctuates between 10^4 and 5×10^5 at a wavelength of 4 μm. To examine the influence of the grating height on the polarization sensitivity of the SM-polarizer, T_{TM}, T_{TE}, and ER were analyzed as the grating height increased from 120 to 400 nm at w = 0.2 μm and t_d = 0.2 μm, as shown in Figure 1d–f. High T_{TM} (>0.8) was achieved for grating heights above 200 nm over the entire MWIR range of 3–5 μm. When the grating height was increased to 400 nm, T_{TM} extended to the wavelength range of 2.1–9.5 μm. The T_{TE} spectra were almost independent of the increase in grating height from 120 and 400 nm, as shown in Figure 1e.

Thus, the ER (Figure 1f) remained constant in the mid-wavelength range regardless of the change in the grating height. The aspect ratio (grating height/width of upper grating) of the grating structure also increased, which made fabrication via thermal NIL more difficult, owing to the reduced bending stiffness, which is proportional to the third power of the grating height.[39] Figure 1g–i shows the T_{TM}, T_{TE}, and ER spectra of the SM-polarizer, plotted as a function of the wavelength and duty cycle for t_d = 0.2 μm and t_g = 0.2 μm. When the duty cycle was between 0.5 and 0.65, the T_{TM} (Figure 1g) was higher than 0.8, whereas T_{TE} (Figure 1h) was lower than 10^{-5} over the entire MWIR range. By contrast, the T_{TM} decreased as the duty cycle approached 0 or 1. The T_{TE} was less than 10^{-5} for duty cycles between 0.5 and 0.65 in the MWIR range, and the ER (Figure 1i) was determined to be more than 8.6×10^4. Figure 1j–l shows the T_{TM} and ERs for different spacer thicknesses, grating heights, and duty cycles at a wavelength of 4 μm (center wavelength in the MWIR band), respectively. Both T_{TM} and ER at 4 μm were dominated by strong oscillations caused by the typical F–P resonance, depending on the spacer thickness (Figure 1j). The peak wavelengths of T_{TM} appeared at spacer thicknesses of 0.2, 1.4, 2.6, 3.8, and 5 μm, corresponding to the round-trip propagation phases (γ) of 0, -2π, -4π, -6π, and -8π, respectively. The T_{TM} increased monotonically with the grating height, whereas the ER varied between $1.5–2.1 \times 10^5$ (Figure 1k). Above a grating height of 200 nm, the T_{TM} was larger than 0.95. The T_{TM} initially increased and then decreased after achieving a maximum value of 0.97 (r = 0.6), as r increased from 0.05 to 0.95 (Figure 1l). When the duty cycle was between 0.5 and 0.7, the T_{TM} and ER exceeded 0.95 and 1.5×10^5 at a wavelength of 4 μm, respectively. The grating height and duty cycle were set

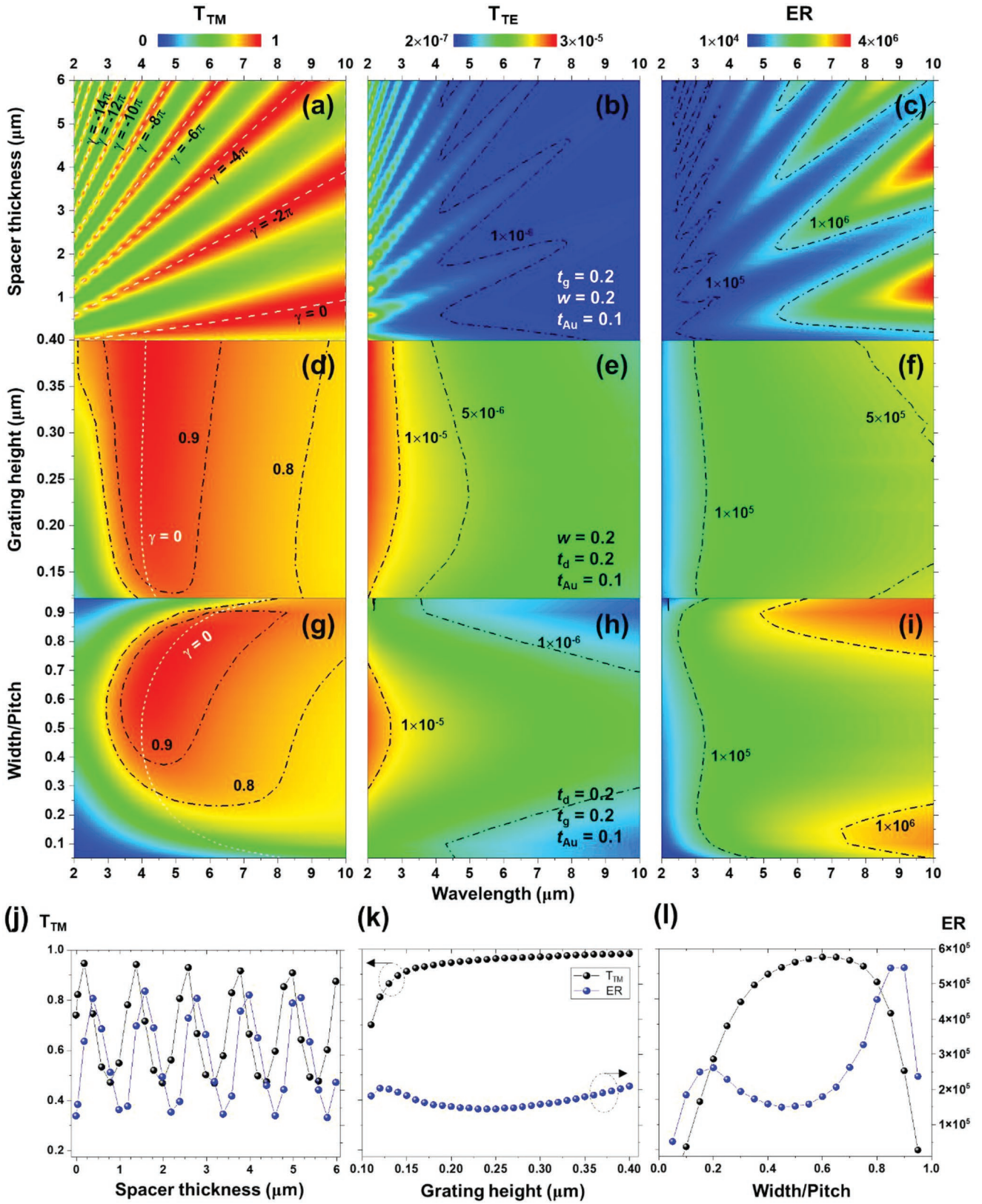

Figure 1. a–i) 2D contour maps of the simulated T_{TM}, T_{TE}, and ER as functions of the spacer thickness (t_d), grating height (t_g), and duty cycle (r) for TM-polarized and TE-polarized incident light at normal incidence. The white dashed lines indicate that the F–P cavity condition is satisfied. The simulated T_{TM} and ER as functions of j) the spacer thickness, k) grating height, and l) duty cycle (Width/Pitch) at a wavelength of 4 μm.

to 200 nm and 0.5, respectively, to accommodate performance variations caused by fabrication imperfections. Other geometric parameters affecting the polarization sensitivity of the SM-polarizer include the pitch, Au thickness, and refractive index of the spacer layer. As the pitch of the grating decreased, the T_{TM} and T_{TE} increased and decreased, respectively, resulting in a higher ER (Figure S2, Supporting Information). When the pitch decreased to 400 nm, the T_{TM} exceeded 0.95 at a wavelength of 4 μm and the ER exceeded 1.5×10^5. At an Au thickness less than 100 nm, the ER was less than 8×10^4, although the T_{TM} exceeded 0.95 at the wavelength of 4 μm (Figure S3, Supporting Information). When the Au thickness exceeded 100 nm, the T_{TM} decreased rapidly while the ER increased above 1.5×10^5, owing to the bilayer grating covered with the Au film. The pitch and Au thicknesses were set to 400 and 100 nm, respectively, which had polarization sensitivities of $T_{TM} > 0.95$ and ER $> 10^5$. Finally, the refractive index of the spacer layer used as the optical cavity was investigated (Figure S4, Supporting Information). The T_{TM} spectra of the SM-polarizer were analyzed in the refractive index range of the spacer layer from 1 to 3.3 at p = 400 nm, w = 200 nm, t_g = 200 nm, and t_{Au} = 100 nm. A spacer thickness that satisfied the F–P resonance condition of $\gamma = 0$ was applied to each refractive index of each spacer. To achieve a T_{TM} above 0.95, the refractive index of the spacer must be in the range of 1–1.7 (e.g., KBr, SiO_2, MgF_2). The sulfur polymer used in this study was found to be a suitable infrared material in this range.

2.2. Preparation of the SM-Polarizer

To achieve a highly polarization-sensitive SM-polarizer, the elemental sulfur (S) content in the poly(S-*r*-DIB) [poly(elemental sulfur–random-1,3-diisopropenyl benzene)], which affects refractive index (n), was determined by considering the effective n_{spacer} from the simulation results as well as processability. As mentioned previously, the simulation revealed that the optimal n_{spacer} to achieve a T_{TM} above 0.95 was in the range of 1.0–1.7, indicating that the sulfur content during the synthesis of the poly(S-*r*-DIB) must satisfy the refractive index of 1.0–1.7. Previous reports have also established that the refractive index of the poly(S-*r*-DIB) strongly depends on the elemental sulfur content and that the poly(S-*r*-DIB) has a refractive index higher than 1.7 from 633 to 1554 nm for sulfur content greater than 50 wt.%.[5] The poly(S-*r*-DIB) with sulfur content less than ≈50 wt.% can be prepared using carbon-based organic solvents such as 1,2-dichlorobenzene (DCB), enabling the use of facile polymer processing approaches such as spin-coating, dip-coating, painting, and roll-to-roll coating. Therefore, for the formulation of polymeric sulfur, we used 40 wt.% of elemental sulfur and 60 wt.% of DIB (poly(S_{40}-*r*-DIB_{60})), to ensure satisfactory optical performance and processability.

For the synthesis of poly(S_{40}-*r*-DIB_{60}), elemental sulfur was melted at 185 °C, which is higher than its floor temperature of 159 °C. DIB was added to the molten sulfur, and polymerization was conducted at 185 °C for 8 min (**Figure 2**a). The orange-colored molten sulfur liquid transformed into dark-red-colored poly(S_{40}-*r*-DIB_{60}) during polymerization (Figure S5, Supporting Information). According to the differential scanning calorimetry (DSC) thermogram of the 2nd heating cycle, poly(S_{40}-*r*-DIB_{60}) had a glass transition temperature of (T_g) of 27 °C, without any melting peak, for 8 min of polymerization (Figure S6, Supporting Information). The poly(S_{40}-*r*-DIB_{60}) was quenched by liquid nitrogen to grind into a fine powder, and the poly(S_{40}-*r*-DIB_{60}) powder was dissolved in the DCB at 160 °C for 10 min with concentrations ranging from 0.20 to 1.85 g mL^{-1} (Figure S7, Supporting Information). The poly(S_{40}-*r*-DIB_{60})/DCB solution was spin-coated on a Si wafer, followed by vacuum baking at 160 °C for 20 min to eliminate the residual DCB solvent in the poly(S_{40}-*r*-DIB_{60}) thin film. The vacuum baking was performed to effectively remove the residual DCB at a temperature lower than the boiling temperature of DCB (180 °C) to prevent bubbling defects resulting from rapid boiling (Figure 2b(i)). The thickness of the spin-coated poly(S_{40}-*r*-DIB_{60}) films on the Si wafer could be controlled from 134 to 5370 nm by adjusting the concentrations of the poly(S_{40}-*r*-DIB_{60})/DCB solution from 0.20 to 1.85 g mL^{-1} at a fixed spin speed (Figure S8a–b, Supporting Information). Furthermore, the thickness of spin-coated poly(S_{40}-*r*-DIB_{60}) film can also be controlled by adjusting the spin-speed (Figure S9a–b, Supporting Information). During spin coating, when the spin-speed was changed from 2000 to 8500 rpm while the concentration of the poly(S_{40}-*r*-DIB_{60})/DCB solution was fixed at 0.4 g mL^{-1}, the thickness of spin-coated poly(S_{40}-*r*-DIB_{60}) was reduced from 436 to 363 nm and almost saturated. Hence, a variation in concentration of poly(S_{40}-*r*-DIB_{60})/DCB solution provided a wider range of the thickness control for poly(S_{40}-*r*-DIB_{60}) film in comparison with the spin-speed variation during spin-coating. Hence, we mainly controlled the concentration of poly(S_{40}-*r*-DIB_{60}) solution with fixed 8500 rpm of spin-speed to achieve a wide range of spacer thickness variation. The refractive index of poly(S_{40}-*r*-DIB_{60}) was also defined as a function of wavelength and compared to refractive indices of previously reported the poly(S-*r*-DIB)s with different sulfur contents (50–80 wt.%, 10 wt.% interval) (Figure S10a–b, Supporting Information). The spin-coated poly(S_{40}-*r*-DIB_{60})s prepared by using different concentration of poly(S_{40}-*r*-DIB_{60})/DCB solution show negligible deviation of refractive index among samples originating from its polydisperse molecular weight. The refractive index at fixed wavelength of poly(S_{40}-*r*-DIB_{60}) is well matched with rule of mixtures depending on the sulfur weight percent in poly(S-*r*-DIB).

After the spin-coating process for the thickness-controlled spacer, 1D nano-gratings integrated with spacer layer based on the poly(S_{40}-*r*-DIB_{60}) (poly(S_{40}-*r*-DIB_{60}) 1D nano-gratings) were fabricated via the thermal NIL process (Figure 2b(ii); Figure S11, Supporting Information). We prepared a thermally stable thermal NIL stamp with high fidelity 1D nano-gratings by replica-molding the Si master mold using UV-curable Ormo-Stamp.[40] To support the Ormostamp layer, a poly(ethylene terephthalate) (PET) film was adapted as a rigid substrate for the thermal NIL stamp. A poly(dimethylsiloxane) (PDMS) layer was employed to apply uniform pressure during the thermal NIL process. After the thermal NIL, the imprinted poly(S_{40}-*r*-DIB_{60}) was cooled below the T_g (27 °C) of poly(S_{40}-*r*-DIB_{60}) to produce the poly(S_{40}-*r*-DIB_{60}) 1D nano-gratings. A structural color sequence can be reflected from the periodic nano-structures

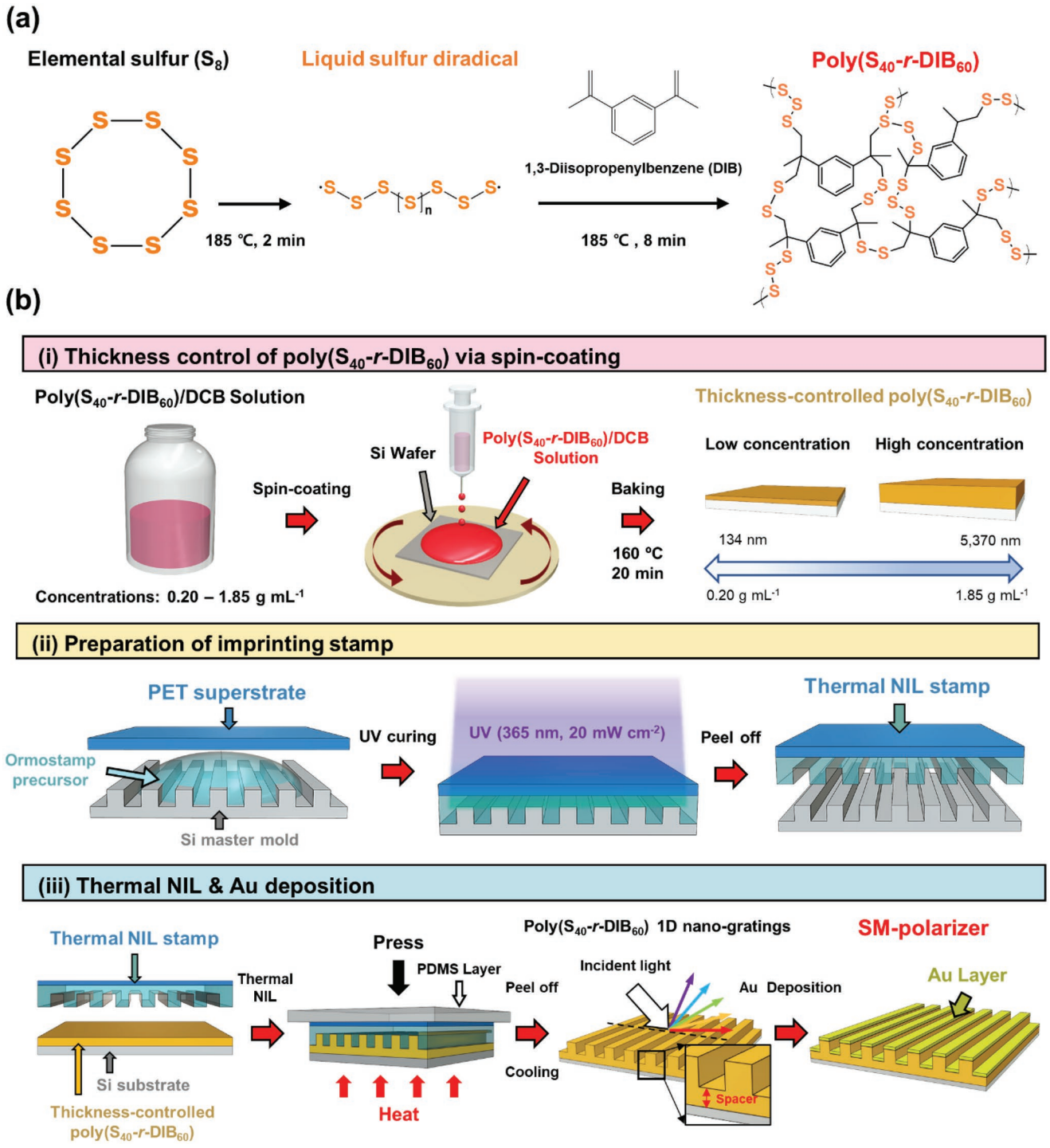

Figure 2. a) Schematic illustration of the synthesis of poly(S_{40}-*r*-DIB$_{60}$). b) Schematic illustration of the preparation of the SM-polarizer. i) Preparation of thickness-controlled spin-coated poly(S_{40}-*r*-DIB$_{60}$) on a Si wafer. The thickness of the spin-coated poly(S_{40}-*r*-DIB$_{60}$) is controlled by using different concentrations of the poly(S_{40}-*r*-DIB$_{60}$)/DCB solution. ii) Preparation methods of the thermal NIL stamp. A PET film is employed as a superstrate of the thermal NIL stamp to support Ormostamp layer. iii) Thermal NIL and Au deposition on the thickness-controlled poly(S_{40}-*r*-DIB$_{60}$) film to prepare the SM-polarizer. A PDMS layer is used to apply uniform pressure over the entire area of the poly(S_{40}-*r*-DIB$_{60}$) film during thermal NIL.

of the poly(S_{40}-*r*-DIB$_{60}$) 1D nano-gratings. The fabrication of the SM-polarizer was completed after deposition of Au on the poly(S_{40}-*r*-DIB$_{60}$) 1D nano-gratings (Figure 2b(iii)). Additional information on the materials and preparation methods are provided in the Experimental section and the Supporting Information.

2.3. Spacer-Thickness-Tailored SM-Polarizer with High-Fidelity 1D Nano-Gratings

2.3.1. Investigation of Thermal NIL Conditions for Constructing High-Quality Poly(S_{40}-r-DIB_{60}) 1D Nano-Gratings

To fabricate a highly polarization-sensitive SM-polarizer, a high-quality thermal NIL stamp must be prepared prior to conducting thermal NIL. During preparation of thermal NIL stamp, the Ormotamp precursor is dropped onto the Si master mold and pressed with PET film to fill the nano-cavity of the master mold. If the trapped air in nano-cavity of master mold is not completely removed during filling of the Ormostamp precursor, the resulted thermal NIL stamp has rounded upper gratings after UV curing. In this instance, low-quality thermal NIL stamps can result wherein the Ormostamp precursor has insufficiently filled the cavity of the master mold during preparation of thermal NIL stamp (Figure S12a, Supporting information). There are four possible geometries of the thermally imprinted 1D nano-gratings (**Figure 3**a). Figure 3a(i,ii) depicts the possible geometries of the thermally imprinted 1D nano-gratings prepared using a low-quality thermal NIL stamp. Round-shape lower gratings in the poly(S_{40}-*r*-DIB_{60}) 1D nano-gratings were generated owing to the round-shape upper gratings in the low-quality thermal NIL stamps, regardless of the suitability of the thermal NIL conditions (Figure S12b, Supporting Information). Therefore, the high-quality thermal NIL stamp was required in advance to prevent round-shape lower gratings in the poly(S_{40}-*r*-DIB_{60}) 1D nano-gratings.

While using a high-quality thermal NIL stamp, the quality of the resulting 1D nano-gratings highly depends on the suitability of the thermal NIL conditions. Hence, investigation of thermal NIL conditions including imprinting pressure, temperature, and time are required for overcoming the energy barrier of the Cassie–Baxter state, originating from the high surface tension and viscosity of poly(S_{40}-*r*-DIB_{60}). At the beginning of the thermal NIL, the poly(S_{40}-*r*-DIB_{60}) film was in the unfilled Cassie–Baxter state. Ideally, the final result from the thermal NIL process is the fully filled Wenzel state. When the energy barrier cannot be overcome because of the unsuitable thermal NIL conditions, the polymeric sulfur cannot fill the cavity of the thermal NIL stamp, resulting in an incompletely filled upper gratings, called the intermediate state (Figure 3a(iii); Figure S12c, Supporting Information). When the Au deposition is conducted onto low-fidelity poly(S_{40}-*r*-DIB_{60}) 1D nano-gratings with round-shape upper gratings, the resulting upper Au layer has the same round-shape (Figure S13a, Supporting Information). The round-shape of upper Au layer reduces the gap between upper and lower Au layers which deteriorates the ER due to reduced T_{TM}. According to simulation results, it is clear that the low-fidelity of the poly(S_{40}-*r*-DIB_{60}) 1D nano-gratings adversely affects the T_{TM}, T_{TE}, and ER of the SM-polarizer (Figure S13b–d, Supporting Information). As the edge radius increases (i.e., SM-polarizer with low fidelity 1D nano-gratings), the T_{TM} decreases rapidly compared to the SM-polarizer with high-fidelity 1D nano-gratings. For this reason, to avoid the intermediate state and achieve the Wenzel state, the energy barrier of the Cassie–Baxter state can be significantly reduced by applying higher thermal NIL temperatures, which can simultaneously reduce the surface tension and viscosity. Imprinting time is an important processing parameter in the thermal NIL of polymeric materials, because of time-dependent viscoelasticity of the poly(S_{40}-*r*-DIB_{60}) film on Si wafer. Therefore, to achieve high-fidelity poly(S_{40}-*r*-DIB_{60}) 1D nano-gratings, a high-quality thermal NIL stamp and suitable conditions are both required to induce a complete Cassie–Baxter-to-Wenzel transition (Figure 3a(iv) and Figure 3b).

Before a systematic investigation of the thermal NIL conditions, the Ormostamp/PET thermal NIL stamp was prepared as a high-quality replica of the master mold with the 1D nano-gratings (Figure S14, Supporting Information). The first imprinting was performed under a fixed imprinting temperature of 80 °C, corresponding to ~T_g + 50° where typically shows rubbery plateau. The imprinting time was systematically adjusted to 60, 90, and 120 min at a fixed imprint pressure of 15 kgf cm^{-2}. At 80 °C, under 15 kgf cm^{-2} of pressure, 120 min of imprinting time was required to obtain high-fidelity poly(S_{40}-*r*-DIB_{60}) 1D nano-gratings, which is excessively long for practical applications (Figure 3c(i)). Therefore, a temperature higher than 80 °C was deemed necessary to reduce the activation energy of the Cassie–Baxter-to-Wenzel transition and lower the imprinting time. To identify the appropriate temperature range, the degradation behavior of poly(S_{40}-*r*-DIB_{60}) was measured by thermal gravimetric analysis (TGA, Figure S15, Supporting Information). The poly(S_{40}-*r*-DIB_{60}) exhibited an onset decomposition temperature ($T_{d,5wt.\%}$) of 195 °C under an air atmosphere with a heating rate of 20 °C min^{-1}. An isothermal test was also conducted under air to investigate the time-dependent thermal degradation behavior of poly(S_{40}-*r*-DIB_{60}) below the $T_{d,5wt.\ \%}$. At 110 °C, the weight loss of poly(S_{40}-*r*-DIB_{60}) was found to be less than 0.3 wt.% over 15 min of the isothermal test. The thermal NIL was conducted at 110 °C by systematically increasing the imprinting pressure to 10, 15, and 20 kgf cm^{-2} over 10 min (Figure 3c(ii)). Above 15 kgf cm^{-2} at 110 °C, a high-fidelity poly(S_{40}-*r*-DIB_{60}) 1D nano-grating was successfully obtained with a significantly shorter imprinting time of 10 min compared to the 120 min required at 80 °C and an imprinting pressure of 15 kgf cm^{-2}.

To further enhance processing efficiency, an additional precise control of thermal NIL conditions was performed. The imprinting time was adjusted from 10 to 5 min, and the imprinting pressure was elevated from 15 to 30 kgf cm^{-2} to compensate for the reduced imprinting time and prevent less-filled results with low fidelity, according to Stefan's squeeze-flow equation (Equation 2).[41]

$$\frac{1}{h(t)^2} = \frac{1}{h_0^2} + \frac{2p}{\eta w^2} t \tag{2}$$

where $h(t)$, h_0, p, η, w, and t are the grating height, initial thickness, applied pressure, viscosity, grating width, and thermal imprinting time, respectively. The thermal NIL temperature was also adjusted from 110 to 100 °C, considering the thermomechanical properties of the PET layer in the thermal NIL stamp to prevent undesirable defects resulting from thermal deformation of the thermal NIL stamp. From the maximum tan δ of the dynamic mechanical analysis (DMA) temperature sweep test, the glass transition temperature of the PET superstrate

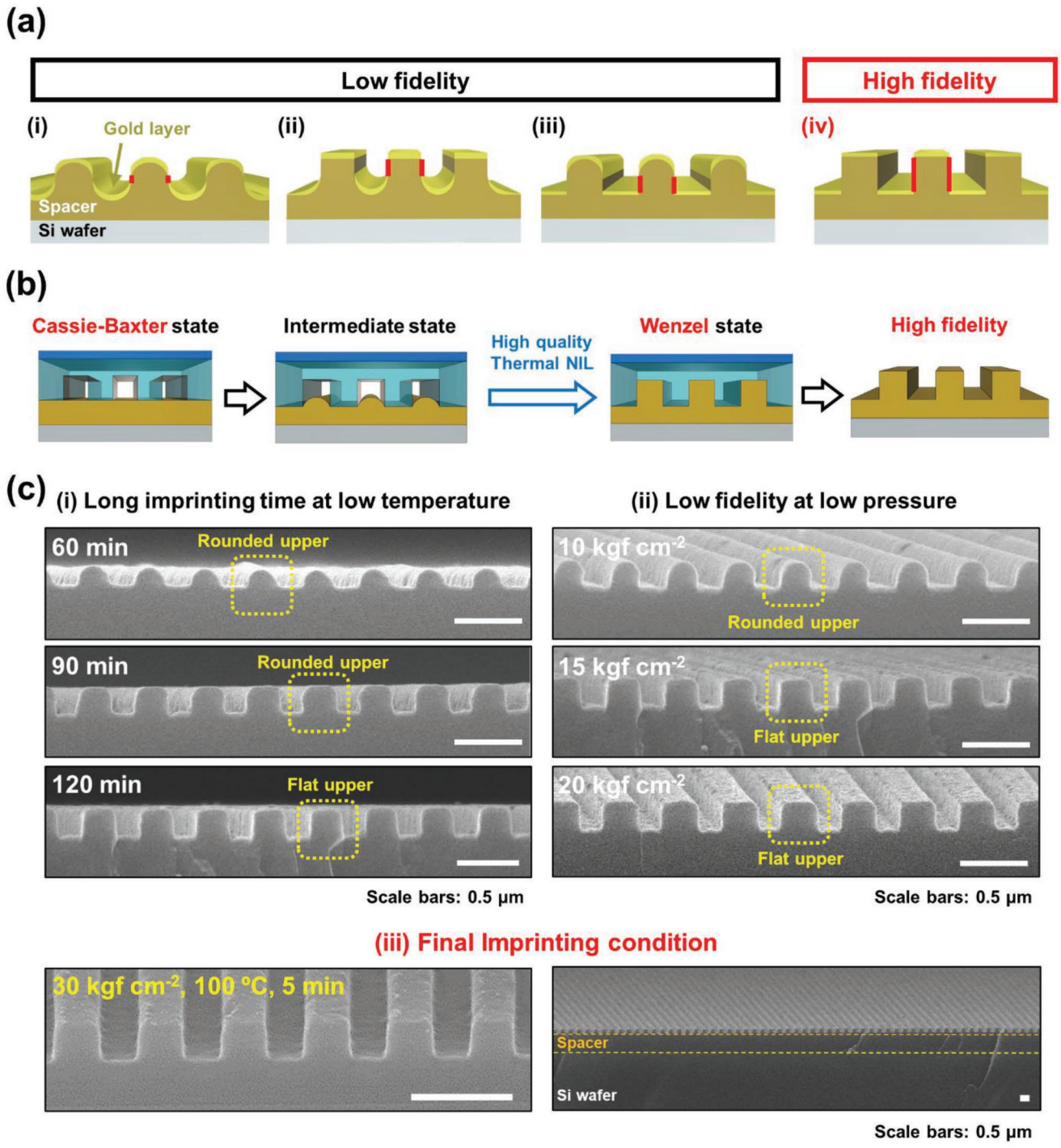

Figure 3. a) Schematic illustrations of SM-polarizers with four possible geometries. Low fidelity: i) rounded upper and rounded lower gratings, ii) flat upper and rounded lower gratings, and iii) rounded upper and flat lower gratings. High fidelity: iv) flat upper and flat lower gratings. The red line indicates the gap between the upper and lower gratings. b) Schematic illustration of the formative principle of the high-fidelity poly(S_{40}-*r*-DIB_{60}) 1D nano-gratings during thermal NIL. c) SEM images of poly(S_{40}-*r*-DIB_{60}) 1D nano-gratings fabricated using i) Three different thermal NIL times at a fixed pressure of 15 kgf cm^{-2} and temperature of 80 °C and ii) Three different NIL pressures (10, 15, and 20 kgf cm^{-2}) at a fixed temperature of 110 °C and imprinting time of 10 min. iii) High- and low-magnitude SEM images of poly(S_{40}-*r*-DIB_{60}) 1D nano-gratings fabricated under the final thermal NIL conditions—a pressure of 30 kgf cm^{-2}, a temperature of 100 °C, and an imprinting time of 5 min.

was determined to be 116 °C (Figure S16, Supporting Information), which is close to the immediately preceding imprinting temperature of 110 °C, because the glass transition is a broad second-order transition. The storage modulus (E′) of the PET, which exhibits resistance to external deformation, was determined to be 1995.6 and 1491.5 MPa at 100 and 110 °C,

respectively, indicating that a process temperature of 100 °C better ensures the thermomechanical durability of the thermal NIL stamps than 110 °C. Furthermore, the thermal decomposition and denaturalization of poly(S_{40}-*r*-DIB_{60}) were prevented by simultaneously reducing the time and temperature. Finally, high-fidelity poly(S_{40}-*r*-DIB_{60}) 1D nano-gratings were achieved over an area of 1 × 1 cm^2 by applying thermal NIL conditions of 30 kgf cm^{-2} at 100 °C for 5 min, as demonstrated by cross-sectional and tilted SEM images (Figure 3c(iii)).

For the SM-polarizer, the Au deposition was conducted immediately after the thermal NIL process on the poly(S_{40}-*r*-DIB_{60}) 1D nano-gratings at 30 kgf cm^{-2} and 100 °C for 5 min. The Au layers, located on the upper and lower gratings of poly(S_{40}-*r*-DIB_{60}) 1D nano-gratings, were separated without physical connection owing to the nearly right-angled nano-gratings, as evident from the SEM images (**Figure 4**a). Furthermore, the SM-polarizer reflected incident white light to an angle-dependent structural color sequence, indicating the successful application of the uniform periodic 1D nano-gratings to the preparation of the SM-polarizer. The RGB values from the digital images of the structural color reflection at various set angles were converted to XYZ values and plotted in the CIE 1931 space (Figure S17, Supporting Information). In addition to the high-quality imprinting of the 1D nano-grating, a suitable spacer thickness is important for achieving high polarization sensitivity. According to the simulation results in Figure 1a, the

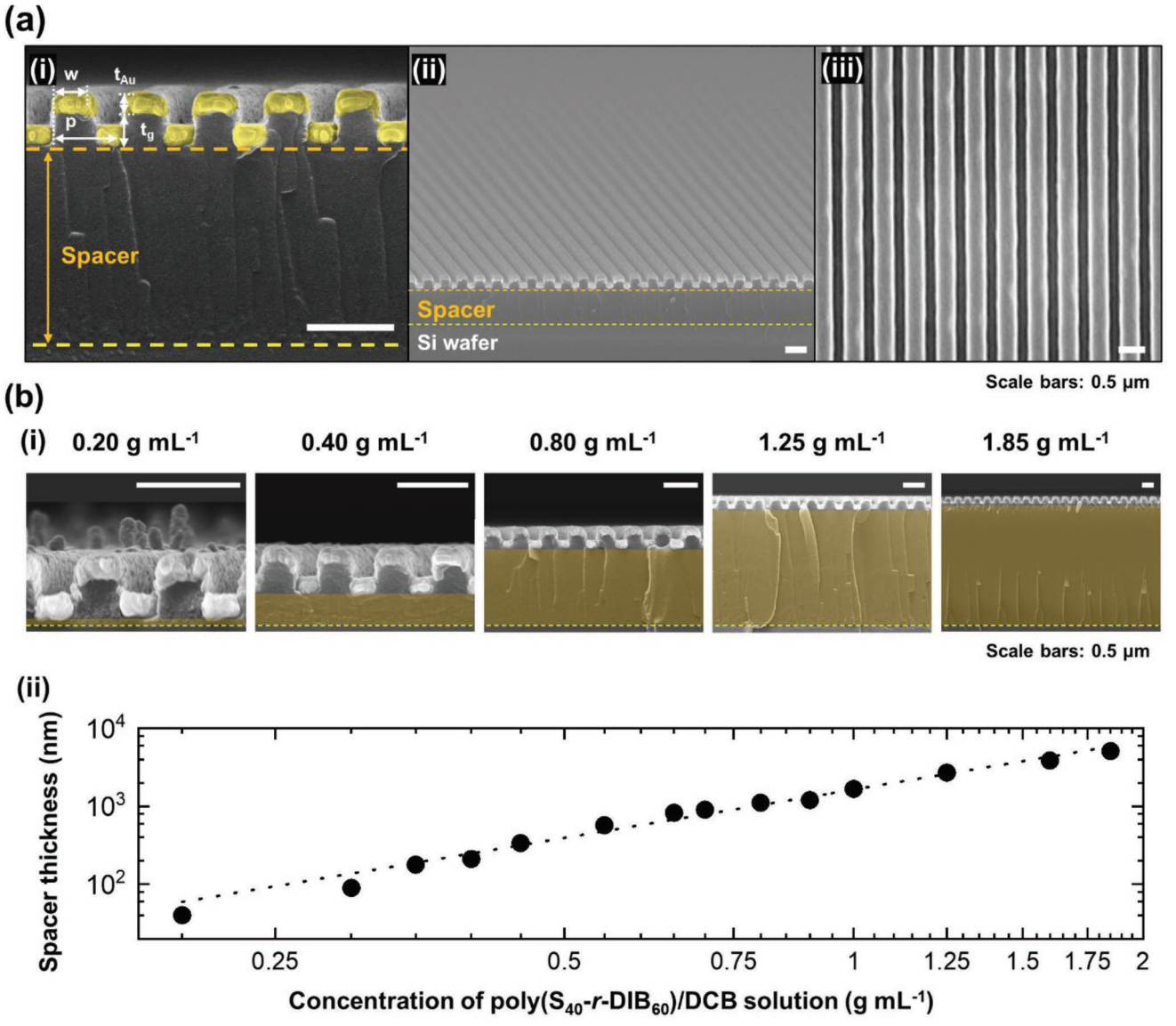

Figure 4. a) SEM images of the SM-polarizer. i) Cross-sectional view. The yellow regions indicate the Au-deposited layer. ii) Tilted view. iii) Top-down view. (*w*: Width of upper grating, t_g: Grating height, *p*: Pitch, and t_{Au}: Thickness of the Au layer). b) Cross-sectional SEM images of i) the SM-polarizer fabricated by using different concentrations of the poly(S_{40}-*r*-DIB_{60})/DCB solution. The orange-colored regions in the SEM images indicate the spacer layer of the SM-polarizer. ii) Spacer thickness of the SM-polarizer is plotted as a function of applied the concentration of the poly(S_{40}-*r*-DIB_{60})/DCB solution during preparation.

0th F–P order provided a high T_{TM} in the broadband MWIR region, suggesting that the spacer thickness of the SM-polarizer should be tailored to ensure the 0th F–P order for a high polarization sensitivity. To tailor the spacer thickness of the SM-polarizer, we increased the concentration of the poly(S_{40}-*r*-DIB_{60})/DCB solution from 0.20 to 1.85 g mL^{-1} for the spin-coating process. Cross-sectional SEM images indicated an increase in spacer thickness according to increase in applied concentration of the poly(S_{40}-*r*-DIB_{60})/DCB solution (Figure 4b(i); Figure S18, Supporting Information). The spacer thickness of the SM-polarizer increased from 40 nm at 0.20 g mL^{-1} to 5100 nm at 1.85 g mL^{-1} (Figure 4b(ii)). Thus, the desired control of F–P resonance were achieved in the SM-polarizer by tailoring the spacer thickness via facile conventional spin-coating.

2.4. Spacer-Thickness-Dependent Polarization Performance of the SM-Polarizer

To determine the polarization sensitivity of the designed SM-polarizer structure based on simulations and theoretical calculations, we measured the T_{TM} and T_{TE} for the fabricated SM-polarizers using a Fourier transform infrared (FT-IR) spectrometer. **Figure 5**a shows the measured T_{TM} spectra of

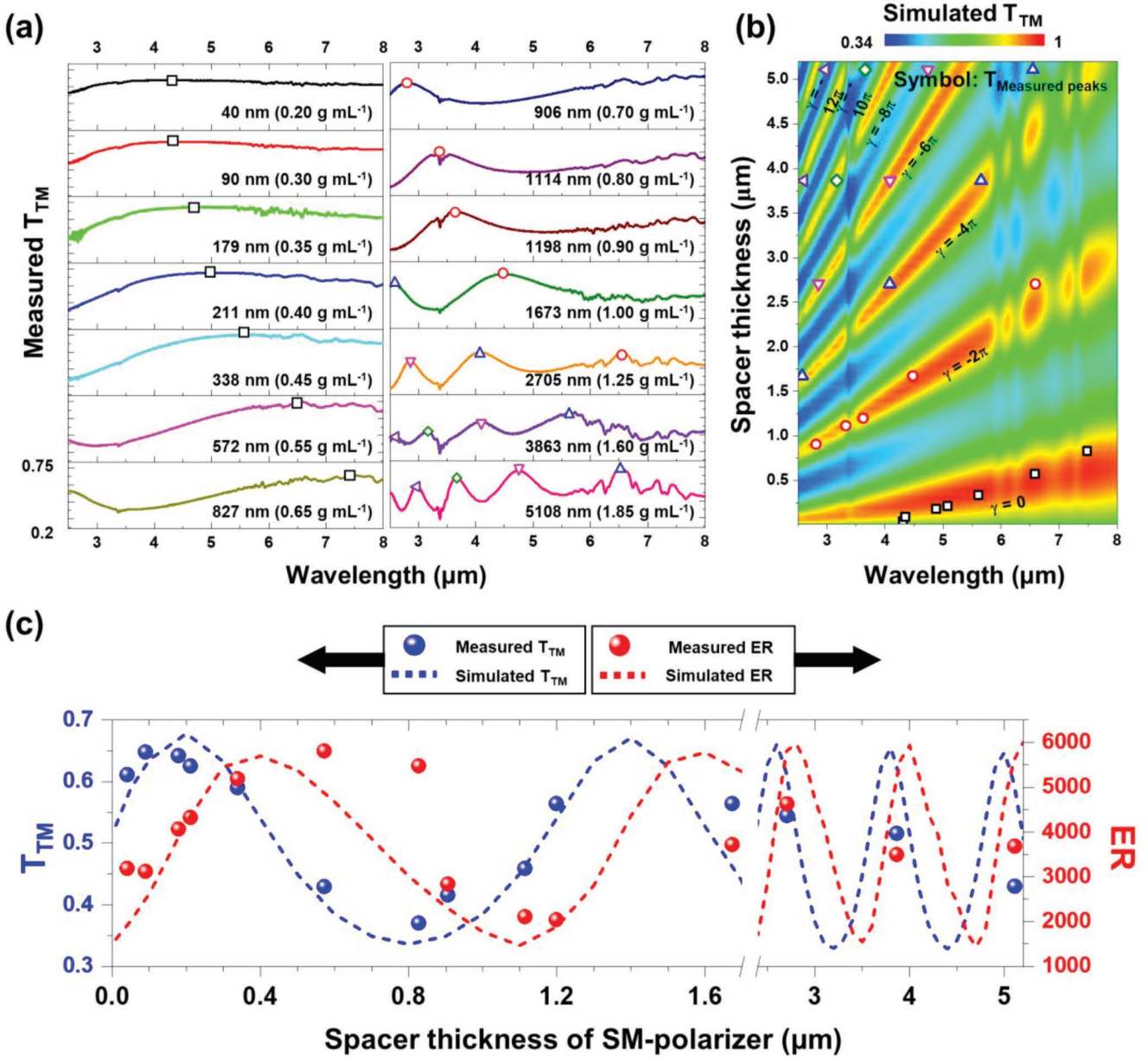

Figure 5. a) FT-IR-measured TM-transmission spectra of SM-polarizer with controlled spacer thickness, fabricated using different concentrations of the poly(S_{40}-*r*-DIB_{60})/DCB solution. b) Simulated T_{TM} color maps for different thicknesses of spacer layer in the SM-polarizer with $p = 0.4$ μm, $w = 0.2$ μm, $t_g = 0.2$ μm, and $t_{Au} = 0.1$ μm. The symbols indicate the peak wavelengths of the measured T_{TM} data corresponding to the F–P cavity resonance mode. c) Simulated and measured T_{TM} and ER of the SM-polarizer as functions of the spacer thickness at 4 μm wavelength. The dashed lines and symbols indicate the simulation and measurement results, respectively.

the SM-polarizers (p = 400 nm, w = 200 nm, t_g = 200 nm, and t_{Au} = 100 nm) with different spacer thicknesses (measured T_{TE} spectra can be found in Figure S19, Supporting Information). As the spacer thickness increased from 40 to 827 nm, only the 0th F–P resonance occurred, and the peak wavelength red-shifted from 4.31 to 7.48 μm. At spacer thicknesses above 827 nm, higher-order resonances appeared in sequence. For spacer thicknesses of 40, 90, 179, 211, 338, 572, and 827 nm, peak wavelengths (maximum T_{TM}) were observed at 4.31 (0.61), 4.35 (0.65), 4.88 (0.64), 5.08 (0.63), 5.61 (0.59), 6.58 (0.43), and 7.48 (0.37) μm, respectively. Notably, the transmission of the Si substrate without an anti-reflective coating was 0.54. Figure 5b shows the simulated T_{TM} of the SM-polarizer structure as functions of the spacer thickness and wavelength. The symbols indicate the measured peak wavelengths; the black-, red-, blue-, magenta-, olive-, and violet-colored symbols correspond to the round-trip propagation phases of 0π (m = 0), -2π (m = 1), -4π (m = 2), -6π (m = 3), -8π (m = 4) and -10π (m = 5), respectively, which satisfy the F–P resonance conditions. The experimental results (Figure 5a) and numerical simulation (Figure 5b) for the peak wavelengths of the SM-polarizer with various spacer thicknesses were consistent. Figure 5c shows the simulated and measured T_{TM} and ER of the SM-polarizer for different spacer thicknesses, t_d. Owing to the mismatch of the T_{TM} and T_{TE} spectra (Figure 1a), ER was shifted by 200 nm with respect to the T_{TM}, whereas the spacer thickness increased. The optimal spacer thickness was 200 nm according to the numerical analysis, yielding the highest T_{TM} and correspondingly high ER at the wavelength of 4 μm. By contrast, the optimal spacer thickness for a high ER was 400 nm. The measurement results showed that the T_{TM} and ER for t_d = 179 nm were 0.60 and 4070, respectively. The SM-polarizer with a spacer thickness of 90 and 572 nm exhibited the highest T_{TM} of 0.65 with ER of 3121, and the highest ER of 5810 with a T_{TM} of 0.43, respectively, among the prepared real samples at 4 μm wavelength. At a spacer thickness of 338 nm, both high T_{TM} and ER of 0.59 and 5190 were obtained at the same 4 μm. Thus, a high T_{TM} and ER can be obtained for an SM-polarizer by controlling the spacer thickness, t_d, between 90–572 nm. Finally, we summarize the geometric parameters and their corresponding T_{TM} and ER of the SM-polarizers (spacer thickness: 90, 338, and 572 nm), and previously reported polymeric sulfur-based polarizers in Table S1 (Supporting Information).

3. Conclusion

In this study, we developed a polymeric-sulfur-based MWIR linear polarizer (SM-polarizer), composed of self-aligned Au gratings (upper and lower) on polymeric sulfur-based 1D gratings with spacer layer and an Si substrate. The solution- and thermal-based processabilities of the poly(S_{40}-*r*-DIB_{60}), respectively, provided controllability of spacer thickness and applicability of thermal NIL, which is a relatively facile and cheap process compared with optics-based lithography. During fabrication, the nanoscale spacer thickness was first controlled as a function of the concentration of the poly(S_{40}-*r*-DIB_{60})/DCB solution in a low-cost spin-coating process. Approximately right-angled 1D nano-gratings with controlled spacer thicknesses were fabricated using a systematically tailored thermal NIL process, during which the pressure, temperature, and time were varied, considering the quality of the imprinting results, economic feasibility of the process, and thermal degradation of polymeric sulfur. The preparation of high-fidelity poly(S_{40}-*r*-DIB_{60}) 1D gratings is important for a highly polarization-sensitive SM-polarizer by ensuring physical separation of each self-aligned Au layer after the Au deposition. The SM-polarizer yielded a T_{TM} of 0.65, 0.59, and 0.43 and an ER of 3.12×10^3, 5.19×10^3, and 5.81×10^3 at 4 μm for spacer thicknesses of 90, 338, and 572 nm based on FT-IR measurements. These values are superior to those of commercial polarizers based on semiconductors and chalcogenides such as BaF_2, ZnSe, and KRS-5, which typically have an ER of 0.15×10^3 and a T_{TM} of approximately 0.50–0.65 (Source: Edmund Optics). In particular, the maximum ER (5.81×10^3) at 4 μm of our SM-polarizer was 19.1 times higher than that of previously reported polymeric sulfur-based polarizer (0.30×10^3 of ER). This research can facilitate the application of polymeric sulfur for cost-effective fabrication of waste-based MWIR polarizers with high polarization sensitivities.

4. Experimental Section

Materials: Elemental sulfur (S_8, reagent-grade sublimed powder, Sigma–Aldrich), 1,3-diisopropenylbenzene (DIB, 97%, TCI), 1,2-dichlorobenzene (DCB, anhydrous, 99%, Sigma–Aldrich), trichloro(1H, 1H, 2H, 2H-perfluorooctyl)silane (97%, Sigma–Aldrich), OrmoStamp (Micro Resist Technology GmbH/Microchem Corp.), and a poly(dimethylsiloxane) (PDMS, Sylgard 184, DOW Corning) precursor and crosslinking agent were purchased and used as received.

Synthesis of the Poly(S_{40}-r-DIB_{60}): The elemental sulfur powder (4.0 g) was added to a glass vial with a magnetic stir bar and placed in an oil bath at 185 °C. When elemental sulfur formed a clear orange molten phase, DIB (6.0 g) was injected into it, and the mixture was stirred at 185 °C for 8 min until the formation of deep-red-colored polymeric melt. The poly(S_{40}-*r*-DIB_{60}) was then further reacted in a vacuum oven at 170 °C for 10 min, cooled to room temperature (25 °C), powdered, and stored in a vacuum chamber.

Preparation of the Poly(S_{40}-r-DIB_{60})-Coated Si Wafer: The poly(S_{40}-*r*-DIB_{60}) powder was dissolved in DCB with vigorous magnetic stirring until the formation of a homogeneous deep-red colored solution at 160 °C for 10 min. The poly(S_{40}-*r*-DIB_{60})/DCB solution was then cooled to room temperature (25 °C) and spin-coated (APT Automation GmbH, Spin150i) on a plasma-cleaned double-sided polishing (DSP) silicon (Si) wafer in ambient air. The coating speed was set to 2000 rpm for 15 s with an acceleration rate of 266 rpm s^{-1} and at 8500 rpm for 15 s with an acceleration rate of 665 rpm s^{-1}. The residual solvent of the spin-coated poly(S_{40}-*r*-DIB_{60}) was removed via thermal annealing at 170 °C and normal pressure for 10 min, followed by additional annealing at 170 °C for 10 min under vacuum.

Preparation of the Thermal NIL Stamp: A Si master mold with 1D nano-gratings was patterned using electron beam lithography, followed by conventional reactive-ion etching processes. The Si master mold had a 1D nano-gratings structure with a pitch, width, and height of 400, 200, and 200 nm, respectively. The Si master molds were coated with anti-sticking layers of trichloro(1H, 1H, 2H, 2H-perfluorooctyl) silane for 3 h in a vacuum desiccator. To replicate the nanopattern of the Si master mold, a UV-curable OrmoStamp was dropped onto a Si mater mold with patterned regions. The master mold with the resin was then covered with a plasma-treated polyethylene terephthalate (PET) film and cured via exposure to monochromic 365-nanometer UV light (20 mW cm^{-1}) for 3 min using a collimated UV light (CoolLED, pE-4000).

Finally, the nanopatterned Ormostamp on PET was peeled off the Si master to obtain a flexible polymer mold (i.e., OrmoStamp/PET mold). The thermomechanical properties of the PET film were measured via DMA (TA instruments, Q800). The surface of the Ormostamp-based thermal NIL stamp was also treated with an anti-sticking layer for easy detachment from the poly(S_{40}-*r*-DIB_{60}) 1D nano-gratings after imprinting.

Preparation of the SM-Polarizer: The poly(S_{40}-*r*-DIB_{60}) 1D nano-gratings were fabricated via the thermal nanoimprint method using an OrmoStamp/PET imprinting stamp. The thermal NIL process was performed at 30 kgf cm^{-2} of pressure and 100 °C for 5 min. After the thermal NIL, the system was cooled to room temperature (25 °C) to obtain the poly(S_{40}-*r*-DIB_{60}) 1D nano-gratings. Subsequently, 100 nm (7/86/7 nm) of Au layer was deposited via electron beam evaporation (IVT, E-beam Evaporation System) under vacuum (base pressure <10^{-7} Torr) onto the poly(S_{40}-*r*-DIB_{60}) 1D nano-gratings at deposition rates of 0.2/0.4/0.2 Å s^{-1}.

Optical Characterizations: Spectroscopic ellipsometry measurements were performed to determine the optical properties (refractive index: *n*, and extinction coefficient: *k*) of poly(S_{40}-*r*-DIB_{60}) by using ellipsometer (J. A. Woollam, RC2-DI). Each sample was measured at an incident angle of 70 degrees and spectral range of 400–1000 nm. All transmission measurements were performed by using a Fourier transform infrared (FT-IR) spectrometer (ThermoFisher Scientific, Nicolet 5700) and a liquid-nitrogen-cooled mercury cadmium telluride detector with a KBr beam splitter. Transmission spectra were recorded with a spectral resolution of 4 cm^{-1} in the wavelength range of 2.5–8 µm. The spectrometer was purged continuously with N_2 gas to avoid absorption of CO_2 and H_2O. Commercial infrared (IR) wire-grid polarizers (WGP) were placed in front of the IR source to generate a linearly polarized light with parallel and perpendicular states. The fabricated grating device was then installed and adjusted to be collinear with the linearly polarized incident light. The T_{TE} of the sample was first measured in the TE mode, where the intensity was minimized by vertically configuring the metal grid axis of the fabricated sample and commercial WGP.

Numerical Simulation: Numerical simulations were performed using the commercial finite integration technique simulation tool (CST Microwave Studio). The perfect electric conductor (PEC, $E_t = 0$) and perfect magnetic conductor (PMC, $H_t = 0$) boundary conditions were used for the *xz*-plane and *yz*-plane, respectively. The dielectric functions of bulk Au in the infrared region were described according to the Drude model with a plasma frequency of 1.38×10^{16} Hz and collision frequency of $w_c = 5.71 \times 10^{13}$ Hz. The frequency-independent refractive indices of the silicon substrate and spacer layer were 3.4 and 1.7, respectively. All spacer thicknesses were set according to the experimental values and the sizes determined from the SEM images.

Supporting Information

Supporting Information is available from the Wiley Online Library or from the author.

Acknowledgements

W.C., J.H., and S.Y.L. contributed equally to this work. This work was supported by the Technology Innovation Program (No. 20011153) funded by the Ministry of Trade, Industry & Energy (MOTIE) and Korea Evaluation Institute of Industrial Technology (KEIT) of the Republic of Korea, and the US Air Force Asian Office of Aerospace Research and Development (AOARD; FA2386-22-1-4086), and a grant from the National Research Foundation (NRF) funded by the Korea government (NRF-2022R1A2C2002911).

Conflict of Interest

The authors declare no conflict of interest.

Data Availability Statement

The data that support the findings of this study are available from the corresponding author upon reasonable request.

Keywords

Fabry–Pérot resonance, inverse vulcanization, linear polarizer, mid-wavelength infrared, polymeric sulfur

Received: October 11, 2022
Revised: November 18, 2022
Published online:

[1] W. J. Chung, J. J. Griebel, E. T. Kim, H. Yoon, A. G. Simmonds, H. J. Ji, P. T. Dirlam, R. S. Glass, J. J. Wie, N. A. Nguyen, B. W. Guralnick, J. Park, Á. Somogyi, P. Theato, M. E. Mackay, Y. E. Sung, K. Char, J. Pyun, *Nat. Chem.* **2013**, *5*, 518.
[2] T. S. Kleine, R. S. Glass, D. L. Lichtenberger, M. E. Mackay, K. Char, R. A. Norwood, J. Pyun, *ACS Macro Lett.* **2020**, *9*, 245.
[3] L. E. Anderson, T. S. Kleine, Y. Zhang, D. D. Phan, S. Namnabat, E. A. LaVilla, K. M. Konopka, L. Ruiz Diaz, M. S. Manchester, J. Schwiegerling, *ACS Macro Lett.* **2017**, *6*, 500.
[4] J. J. Griebel, N. A. Nguyen, S. Namnabat, L. E. Anderson, R. S. Glass, R. A. Norwood, M. E. Mackay, K. Char, J. Pyun, *ACS Macro Lett.* **2015**, *4*, 862.
[5] J. J. Griebel, S. Namnabat, E. T. Kim, R. Himmelhuber, D. H. Moronta, W. J. Chung, A. G. Simmonds, K. Kim, J. Van Der Laan, N. A. Nguyen, *Adv. Mater.* **2014**, *26*, 3014.
[6] S. Ha, H. J. Yoon, J. I. Jung, H. Kim, S. Won, J. H. Kwak, H. D. Lim, H. J. Jin, J. J. Wie, Y. S. Yun, *Energy Storage Mater.* **2021**, *37*, 567.
[7] J. J. Griebel, G. Li, R. S. Glass, K. Char, J. Pyun, *J. Polym. Sci. Part A Polym. Chem.* **2015**, *53*, 173.
[8] A. G. Simmonds, J. J. Griebel, J. Park, K. R. Kim, W. J. Chung, V. P. Oleshko, J. Kim, E. T. Kim, R. S. Glass, C. L. Soles, *ACS Macro Lett.* **2014**, *3*, 229.
[9] J. H. Lee, K. H. Kim, M. Choi, J. Jeon, H. J. Yoon, J. Choi, Y. S. Lee, M. Lee, J. J. Wie, *Nano Energy* **2019**, *66*, 104158.
[10] J. Choi, S. Won, H. J. Yoon, J. H. Lee, H. W. Jang, J. Jeon, A. Y. Kim, S. H. Park, J. H. Youk, M. Lee, J. J. Wie, *Nano Energy* **2022**, *92*, 106761.
[11] J. Lim, J. Pyun, K. Char, *Angew. Chemie-Int Ed.* **2015**, *54*, 3249.
[12] J. M. Lee, G. Y. Noh, B. G. Kim, Y. Yoo, W. J. Choi, D. G. Kim, H. G. Yoon, Y. S. Kim, *ACS Macro Lett.* **2019**, *8*, 912.
[13] B. J. Eggleton, B. Luther-Davies, K. Richardson, *Nat. Photonics* **2011**, *5*, 141.
[14] D. A. Boyd, C. C. Baker, J. D. Myers, V. Q. Nguyen, G. A. Drake, C. C. McClain, F. H. Kung, S. R. Bowman, W. Kim, J. S. Sanghera, *Chem. Commun.* **2017**, *53*, 259.
[15] L. L. Yuan, P. R. Herman, *Sci. Rep.* **2016**, *6*, 22294.
[16] Y. Deng, D. Chu, *Sci. Rep.* **2017**, *7*, 5893.
[17] J. Lee, S. Ahn, H. Chang, J. Kim, Y. Park, H. Jeon, *Opt. Express* **2009**, *17*, 22535.
[18] W. Kang, J. Chu, X. Zeng, Y. Fan, *Appl. Opt.* **2018**, *57*, 5230.
[19] T. S. Kleine, N. A. Nguyen, L. E. Anderson, S. Namnabat, E. A. Lavilla, S. A. Showghi, P. T. Dirlam, C. B. Arrington, M. S. Manchester, J. Schwiegerling, R. S. Glass, K. Char, R. A. Norwood, M. E. Mackay, J. Pyun, *ACS Macro Lett.* **2016**, *5*, 1152.
[20] M. Sarkar, D. S. S. Bello, C. Van Hoof, A. J. P. Theuwissen, *IEEE Sens. J.* **2013**, *13*, 1065.
[21] J. S. Tyo, D. L. Goldstein, D. B. Chenault, J. A. Shaw, *Appl. Opt.* **2006**, *45*, 5453.

[22] M. D. Islam, J. O. Kim, Y. Ko, Z. Ku, D. A. Boyd, E. M. Smith, V. Q. Nguyen, J. D. Myers, C. C. Baker, W. Kim, J. S. Sanghera, D. A. Czaplewski, A. M. Urbas, J. Genzer, J. E. Ryu, *Macromol. Mater. Eng.* **2020**, *305*, 2000033.
[23] A. J. Berndt, J. Hwang, M. D. Islam, A. Sihn, A. M. Urbas, Z. Ku, S. J. Lee, D. A. Czaplewski, M. Dong, Q. Shao, S. Wu, Z. Guo, J. E. Ryu, *Polymer (Guildf)* **2019**, *176*, 118.
[24] N. A. Rubin, G. D'Aversa, P. Chevalier, Z. Shi, W. T. Chen, F. Capasso, *Science* **2019**, *364*, eaax1839.
[25] E. Laux, C. Genet, T. Skauli, T. W. Ebbesen, *Nat. Photonics* **2008**, *2*, 161.
[26] J. Hwang, B. Oh, Y. Kim, S. Silva, J. O. Kim, D. A. Czaplewski, J. E. Ryu, E. K. Kim, A. Urbas, J. Zhou, Z. Ku, S. J. Lee, *Sci. Rep.* **2018**, *8*, 6.
[27] S. W. Ahn, K. D. Lee, J. S. Kim, S. H. Kim, J. D. Park, S. H. Lee, P. W. Yoon, *Nanotechnology* **2005**, *16*, 1874.
[28] T.-Y. Yu, N.-C. Chi, H.-C. Tsai, S.-Y. Wang, C.-W. Luo, K.-N. Chen, *Opt. Lett.* **2017**, *42*, 4917.
[29] A. G. Andreou, Z. K. Kalayjian, *IEEE Sens. J.* **2002**, *2*, 566.
[30] K. Maghsoudi, R. Jafari, G. Momen, M. Farzaneh, *Mater Today Commun* **2017**, *13*, 126.
[31] A. C. Liou, R. H. Chen, *Int J Adv Manuf Technol* **2006**, *28*, 1097.
[32] D. Murakami, H. Jinnai, A. Takahara, *Langmuir* **2014**, *30*, 2061.
[33] A. Giacomello, S. Meloni, M. Chinappi, C. M. Casciola, *Langmuir* **2012**, *28*, 10764.
[34] Y. Ekinci, H. H. Solak, C. David, H. Sigg, *Opt. Express* **2006**, *14*, 2323.
[35] K. Jin, W. Zheng, Y. Liu, C. Yang, J. Han, Y. Wang, H. Wang, Q. Liu, F. Huang, *Optik (Stuttg)* **2019**, *199*, 163352.
[36] H. T. Chen, J. Zhou, J. F. O'Hara, F. Chen, A. K. Azad, A. J. Taylor, *Phys. Rev. Lett.* **2010**, *105*, 079902.
[37] CST Studio Suite; Dassault Systemes Simulia Corporation: Providence, RI **2020**.
[38] C. Fowler, J. O. Kim, S. J. Lee, A. Urbas, Z. Ku, J. Zhou, *Adv. Theory Simulations* **2019**, *2*, 1800143.
[39] J. E. Park, J. Jeon, S. J. Park, S. Won, Z. Ku, J. J. Wie, *Small* **2020**, *16*, 2003179.
[40] M. Papenheim, C. Steinberg, K. Dhima, S. Wang, H.-C. Scheer, *J. Vac. Sci. Technol. B, Nanotechnol. Microelectron. Mater. Process. Meas. Phenom.* **2015**, *33*, 06F601.
[41] J. Ryu, H. Lim, S. H. Lee, J. Lee, *Microelectron. Eng.* **2015**, *140*, 67.